Article

Sensing of KCl, NaCl, and Pyocyanin with a MOF-Decorated Electrospun Nitrocellulose Matrix

Lars Lüder,* Peter Niraj Nirmalraj, Antonia Neels, René Michel Rossi, and Michel Calame*

Read Online

ACCESS | Metrics & More | Article Recommendations | Supporting Information

ABSTRACT: Wearable sensors can provide important insight into a patient's health status by monitoring the concentration of specific biomarkers in body fluids. Compared to biofluids such as blood or cerebrospinal fluid, which require an invasive acquisition process, other body fluids such as sweat or exhaled air can be easily collected using patches or masks, sufficient for the detection of metabolic and pathological changes. However, the successful integration of an efficient biosensor into textiles or polymer substrates is a challenge if flexibility and functionality are not to be compromised. Here, we demonstrate the integration of nanoporous metal−organic framework (MOF) particles with nitrocellulose (NC) fibrous layers using an electrospinning approach and validate the efficiency of our MOF@NC structure as biosensors. The chemical response of this hybrid nanomaterial upon exposure to different ionic sweat biomarkers such as NaCl and KCl as well as pyocyanin, a biomarker for the nosocomial pathogen *Pseudomonas aeruginosa*, was investigated using Raman spectroscopy. A change of the Raman intensity at distinct peaks of our MOF-containing architecture occurs after treatment of the material with the analyte solutions. Furthermore, we observed the sensitivities for pyocyanin at the normalized Raman intensity change to be up to −1120 au μm^{-1}, about 4 orders of magnitude larger than for NaCl and KCl. The independence of our architecture from the type of MOF and the possibility of using different MOFs with individual chemistry make this approach a promising platform for versatile and adaptable sensing of biomarkers with high sensitivity and selectivity.

KEYWORDS: metal−organic frameworks, electrospinning, particle integration, Raman spectroscopy, nanoscale, wearable sensor
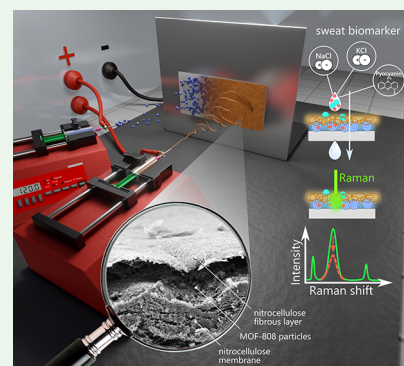
INTRODUCTION

Wearable sensors embedded with stimuli responsive materials are gaining importance in numerous fields from medicine[1,2] to fitness[3,4] and to military applications[5,6] owing to the possibility of collecting and analyzing physicochemical data from individuals with high precision and specificity. Many clinical diagnostic methods necessitate invasive approach to analyze body fluids such as blood,[7−9] cerebrospinal fluid for the detection of neurodegenerative diseases,[10] and tissue samples in diagnosis of cancer.[11] The abundance of biomarkers such as amyloid proteins in these body fluids makes it possible to provide information on a wide range of diseases, but their diversity also makes these body fluids very complex. Other body fluids such as sweat,[12−14] breath,[15,16] saliva,[17,18] or wound exudate[19,20] also contain various biomarkers that reflect the health status of the patient and, unlike body fluids like blood or CSF, can be collected noninvasively by wearables such as patch devices,[21] masks,[22] or wound dressings.[23,24] Equipped with an active biosensing platform, they can accumulate target analytes and detect changes in the concentrations of metabolites, thereby providing information for early diagnosis of existing diseases or observing the course of the condition.

For this purpose, sensors are needed that can meet requirements such as sensitivity, selectivity, and versatility to accurately detect various biomarkers in small quantities.[25] These requirements can be addressed using metal−organic frameworks (MOFs), a relatively new class of nanoporous materials with crystalline coordination structure and extremely large intrinsic surface areas.[26−29] Their versatile structures[30] and tunable functionality[31,32] have made them increasingly important in the field of chemical sensing and biosensing, for example, as a suitable host for specific target analytes.[33−37] Strain-based sensing with MOFs has already demonstrated how the influence of mechanical strain on the MOF structure can be used to detect chemical analytes.[38] Recently, it has already been shown that MOF-based biosensors exhibit remarkable sensing efficiencies with low detection limits, down to the femtomolar range[39−41] for analytes such as heavy metal ions,[42] proteins,[43,44] and cancer biomarkers.[15,40]
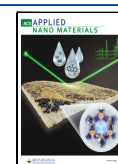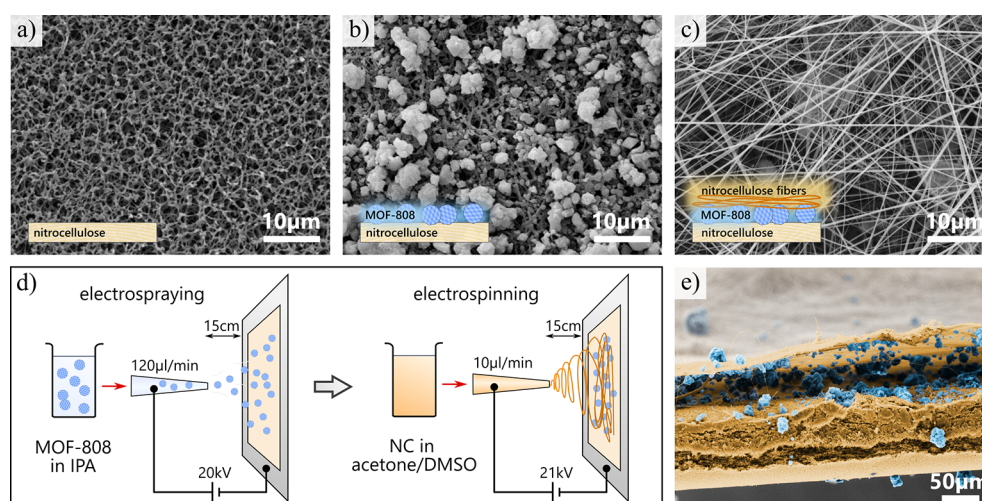
Figure 1. Fabrication of MOF@NC layer. (a−c) Scanning electron microscopy (SEM) images of (a) pure NC membrane and (b) NC membrane with electrosprayed MOF particles and (c) with additional electrospun NC fibrous layer on top. The insets show illustrations of the layer profile. (d) Schematic of sequential electrospraying and electrospinning procedure (objects shown not to scale). By applying a high voltage between the filled syringe and the metal plate electrode, charging effects lead to the release of droplets of MOF suspension or jets of NC polymer solution, respectively, which are deposited on the membrane mounted to the electrode plate. (e) Color coded SEM image of the profile view of the final sandwich structure. Visible delamination and detachment of the top fibrous layer are the result of the cutting process, which was exclusively applied for imaging and profile analysis. MOF particles are colored in blue and NC in orange.

The best method that allows a continuous monitoring process of body fluids such as sweat without jeopardizing the high porosity of MOFs is the integration into porous textiles and polymer membranes for the realization of a wearable sensing platform. However, the integration is a demanding challenge when the functionality of the MOFs should not be lost in the process, such as blocking of the nanopores when coatings are applied over the MOFs. Therefore, for the identification of the target analyte, open access to the MOF should be ensured to enable the specific MOF−analyte interaction as well as access with the analytical tool. Specimen analysis and identification of the target analyte can be realized quickly and label-free by optical Raman spectroscopy[45] based on changes in the individual scattering spectrum due to physicochemical interactions at the molecular level, as it has been shown for sweat sensing,[46] blood analysis,[47,48] cancer detection,[49] or the screening of neurodegenerative diseases from cerebrospinal fluid.[10,50] Raman spectroscopy is gaining traction as a tool for diagnostics: Fast data acquisition based on computational algorithms that reads only the required portion of information increases reading speed and enables scanning of larger areas suitable for biological samples.[51] Furthermore, portable Raman spectroscopy instruments are available that increase mobility and allow on-site analysis, for example, directly on the human body.[52,53] The employment of MOFs in combination with Raman spectroscopy provides advantages such as amplification of the Raman signal or offering selectivity toward specific analytes.[15,34,54]

Here we present the integration of biocompatible MOF-808 particles into nitrocellulose fibrous layers by using a sequential electrospraying and electrospinning procedure. Our approach has the advantage that the active MOF particles are effectively entrapped and held in place by the loose fiber mesh while maintaining the open architecture, thus preserving MOF functionality. The highly porous matrix also provides translucence, which enables the access to optical analytic methods. After demonstrating the fabrication process of the MOF-nitrocellulose nanostructure, scanning electron microscopy

(SEM), atomic force microscopy (AFM), energy dispersive X-ray spectroscopy (EDX), and Raman spectroscopy were used to examine the different membranes. Next, we investigated the optical Raman spectral response of our MOF architectures upon exposure to different ionic sweat biomarkers such as sodium chloride, which is an indicator of cystic fibrosis and sweat rate, as well as potassium chloride, an identifier of muscle activity.[55] To also demonstrate the potential for infection detection, the influence of pyocyanin on our architecture was analyzed. Pyocyanin is released by the nosocomial pathogen *Pseudomonas aeruginosa* as signaling molecule for chemical communication, a phenomenon known as quorum sensing.[56] We anticipate that our integration method could provide a potential route to incorporate MOF particles into textiles, thus having a very practical application for the realization of functional materials and wearable sensing platforms.

■ RESULTS AND DISCUSSION

Fabrication of MOF@NC Structures. The basis for the MOF@nitrocellulose (MOF@NC) architecture is a commercially available nitrocellulose membrane with a pore size of 0.45 μm (manufacturer's information; see Experimental Methods). MOF-808 particles (see Experimental Methods) were integrated by a sequential electrospraying and electrospinning process. First, MOF particles were sprayed and distributed onto the purchased NC membrane. Afterward, electrospinning of NC was executed for several minutes, which led to the formation of a fibrous layer that covered and physically entrapped the MOF particles (see Experimental Methods). The electrospinning time defined the thickness of the fibrous layer; here a time of 20 min was enough to achieve a dense coverage. The fabrication procedure and the resulting layered sandwich structure are shown in Figure 1 and Supporting Information Figure S1. The presented approach has the advantage that one can arbitrarily choose the type of sprayed particles such as different MOFs, as well as the type of electrospun polymer. The flexibility of this method also allows
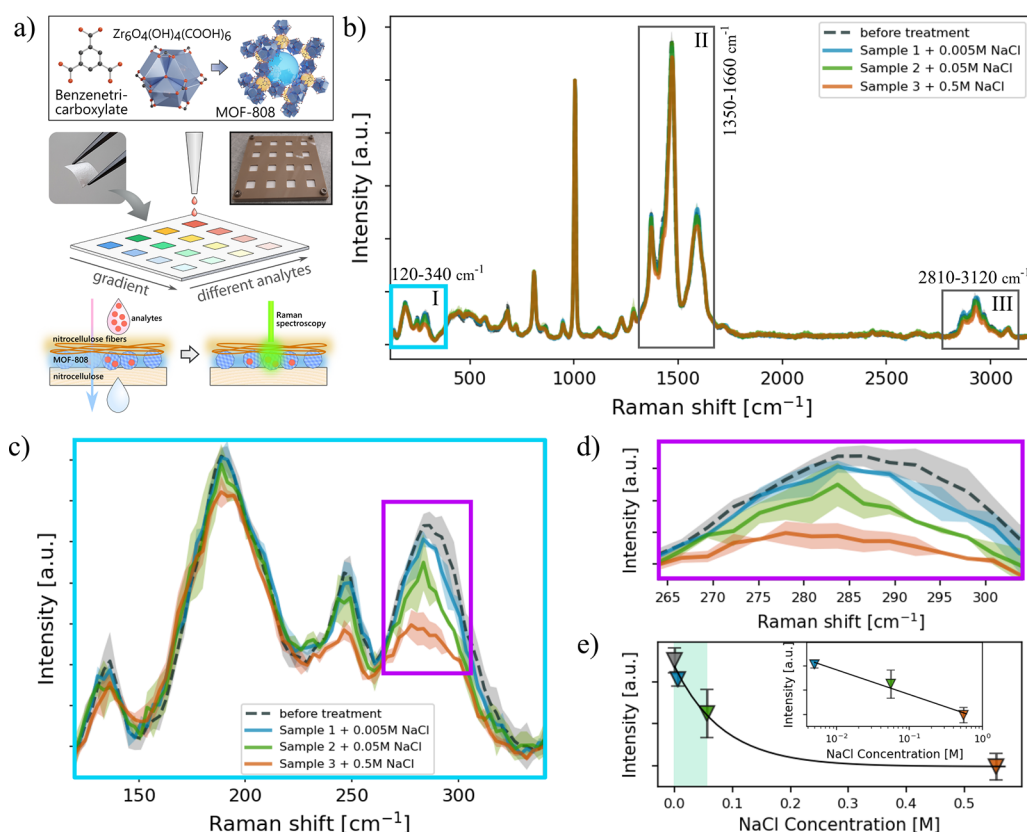
Figure 2. Raman measurements on individual samples after treatment with NaCl (aq). (a) Top: Representation of the molecular structure of benzenetricarboxylate organic linker (BTC) and zirconium metallic cluster, which form MOF-808 after coordination (pores illustrated as blue and yellow spheres). Middle: The fabricated MOF@NC samples are fixed in a sample holder and systematically treated with analytic solutions. Insets show photographs of a tweezer holding MOF@NC sample and a filled sample holder. Bottom: Schematic of the sensing workflow. MOF@NC samples are treated with analyte solution and serve as trap for the added analytes. Raman spectroscopy is performed for chemical analysis and detection of optical signal changes. (b) Full range spectra of individual active MOF@NC samples after treatment with aqueous NaCl solutions of different concentrations (concentrations from 0.005 to 0.5 M, droplet volume of 20 μL, λ_{exc} = 532 nm). Boxes display regions of interest I, II, and III, showing pronounced reduction in signal intensity after addition of NaCl (aq). (c–e) Zoomed-in spectra in region I at 120−340 cm^{-1} (c) and 265−305 cm^{-1} (d), indicated by the cyan and violet box. The solid lines show the average spectra of 11−12 measurements performed on two different samples for each concentration. Colored areas display the standard deviation. (e) Peak intensity values at 286 cm^{-1} for the different treated samples plotted against NaCl concentration. Inset shows the data on a logarithmic scale, and green area highlights the regime of interest, with the linear dependence being further investigated.

the sequences to be adjusted and, if necessary, several layers to be fabricated in series, for example, to create multilayers.

Characterization of the MOF@NC Architecture. X-ray diffraction (XRD) measurements were performed to test the purity of MOF-808. The XRD diffraction pattern showed a clear agreement with known reflections from MOF-808.[57,58] Crystallographic data were obtained from Cambridge Crystallographic Data Center (CCDC), and the simulation of the MOF-808 XRD pattern using CCDC Mercury software resulted in excellent agreement with the measured data (Figure S2a, Supporting Information). Crystallite size of the MOF-808 particles was determined to be 40 ± 5 nm by line profile analysis using the "Williamson-Hall" approach (Figure S2b, Supporting Information).[59]

Energy dispersive X-ray spectroscopy (EDX) measurements were also performed. The mapping of zirconium clearly identified the MOF-808 particles due to the presence of the metal in the cluster (Figure S3, Supporting Information). To test whether the MOF particles are not leached from the fibrous NC layer, the sizes of the MOF particles and the NC mesh spacing were analyzed. To ensure physical entrapment of the particles, the mesh spacing should not be larger than the

particles. For the measurement of the size distribution of the MOF, the particles were sprayed onto a pure aluminum foil. Images were acquired using scanning electron microscopy (SEM) and analyzed using the free computer software Fiji (developed by ImageJ). By applying a brightness threshold, a black and white image was created and the Feret diameters (i.e., the largest dimension) of the particles were calculated (Figure S4, Supporting Information). The possible influence of a treatment with ultrasound for different durations before electrospraying on the particle size distribution was analyzed. Sonication from a minimum of 5 min to a maximum of 60 min was found to have no significant effect on particle size (Figure S5, Supporting Information). No ultrasonication resulted in a less stable suspension with rapid particle precipitation, giving a lower amount of particles in the electrospraying process.

The mesh spacing of the NC fibrous layer was determined in the same way. NC fibers were electrospun on a blank substrate for 20 min and then analyzed by SEM. In the computer software Fiji, the images were converted to black and white, and the outlines of the pores were traced. The calculated Feret diameters of a total of 3263 spacings were evaluated and presented together with the particle sizes (Figure S4,
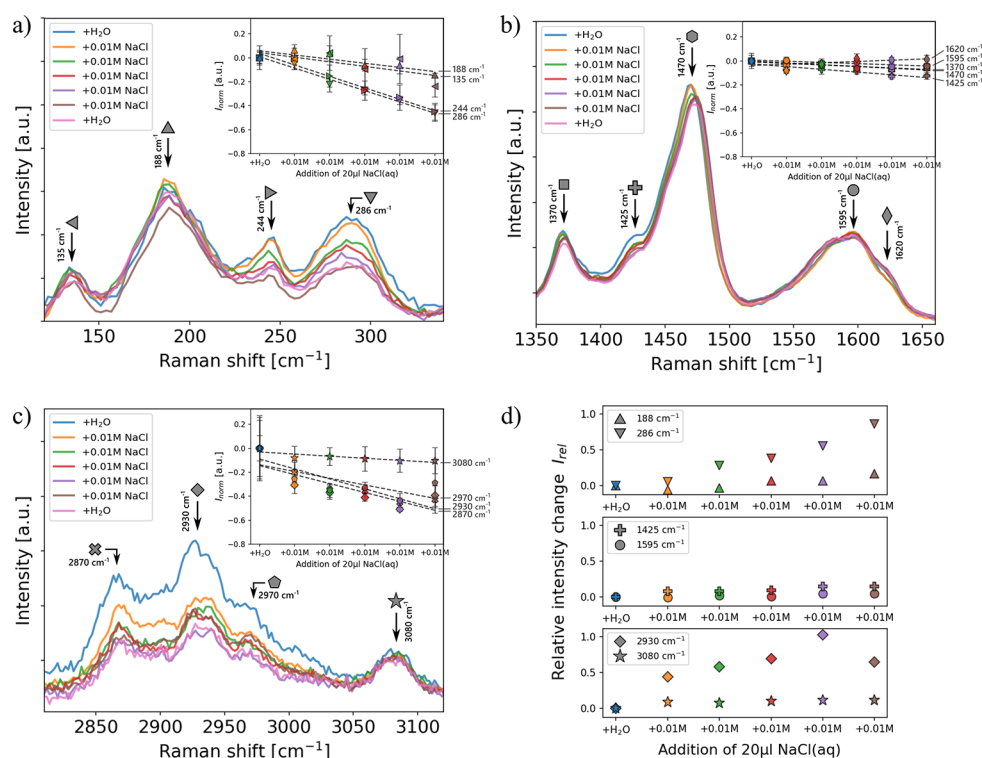
Figure 3. Raman spectra of MOF@NC after successive treatment with H_2O and aqueous NaCl solutions (concentrations of 0.01 M, droplet volume of 20 μL) in the wavenumber regions 120−340 cm^{-1} (a), 1350−1660 cm^{-1} (b), and 2810−3120 cm^{-1} (c). Prominent peaks (marked with symbol and wavenumber) are fitted with a Lorentzian curve, and the normalized intensity change $I_{norm} = \Delta I/I_{H2O}$ (with $\Delta I = I − I_{H2O}$) of the peaks is evaluated and plotted against concentration, shown as inset. The error bars indicate the standard deviation, and the dashed lines show the linear fits. (d) Relative intensity change $I_{rel} = \Delta I/I$ for the peaks with the largest and smallest intensity reduction for each wavenumber region of interest.

Supporting Information). In both cases, an exponential reduction with increasing particle size and mesh spacing is shown, in which the particles tend to be larger than the spacings. Quantification was done by presenting the data as boxplots and determining the median, which is 1.25 μm for the particles and 0.81 μm for the spacing. These benchmark values from the surface analysis are indicators that the tendency of the fibrous layer to have smaller mesh spacing than the MOF particles successfully entraps the particles while presumably providing open access to the MOF pores. The effectiveness of particle entrapment was confirmed by practical leaching tests in which attempts were made to wash out the MOF particles by vigorously stirring the sample in water. Optical inspection of sample and liquid after stirring procedure in SEM microscope showed no visible leaching of particles through the fibrous layer but efficient entrapping by the loose mesh, retaining the MOF functionality and access to optical analysis methods (Figure S7, Supporting Information).

Next, we used Raman spectroscopy to investigate the MOF@NC architectures. The layers were analyzed after each fabrication step, i.e., pure NC membrane, NC membrane with MOF particles, and NC membrane with MOF particles and electrospun fibrous NC layer on top (Figure S8a, Supporting Information). The latter sandwich structure will be referred to as "active" hereafter, as it is the final architecture used for Raman sensing. "Control" samples consisting of a NC fibrous layer on the NC porous membrane without any MOF particles were also prepared and analyzed (see Experimental Methods).

The Raman spectra of MOF and NC are consistent with literature.[58,60] The most prominent peaks are then assigned to the corresponding vibrational modes (Figure S8b, Supporting

Information). In the case of nitrocellulose, the NO and the NO_2 modes are the origin for the signal at wavenumbers 850 cm^{-1} (NO stretching), 1287 cm^{-1} (symmetric NO_2 stretching), and 1660 cm^{-1} (antisymmetric NO_2 stretching).[60] The peak at 1370 cm^{-1} is assumed to be from the cellulose ring.[60] The signal from the MOF mainly stems from the organic benzenetricarboxylate (BTC) ligand. The peaks at 1005 cm^{-1}, 1364 cm^{-1}, and 1592 cm^{-1} can be assigned to the C=C vibrations of the aromatic BTC ring. The signal at 810 cm^{-1} is coming from the C−H out-of-plane deformation mode and at 1470 cm^{-1} from the CO_2^{-} groups.[58] From the spectral analysis of the individual layers, NC and MOF can be clearly distinguished. When viewing the MOF@NC Raman signal, the focal point is adjusted to maximize the MOF signal at 1005 cm^{-1}. At specific wavenumbers we observe higher intensities in the MOF@NC architecture than the pure MOF signal (e.g., 675 cm^{-1}, 9× higher; 715 cm^{-1}, 6× higher; 1287 cm^{-1}, 3.5× higher). It can be attributed to the influence of the superimposed NC top layer that extends into the focal volume of the laser beam and whose spectrum matches that of the peaks. To ensure consistent measurement conditions with fluctuating moisture levels, the following measurements were performed in a closed chamber under a nitrogen atmosphere in which the sample was heated to remove water that had been found to have a masking effect on the MOF Raman signal at low wavenumbers below 300 nm (Figure S8d, Supporting Information).

Sensing Approach. Raman spectroscopy was used as sensing tool, and different analyte solutions were added to active MOF@NC samples to detect changes in the vibrational modes of MOF-808. For this purpose, a sample holder (made
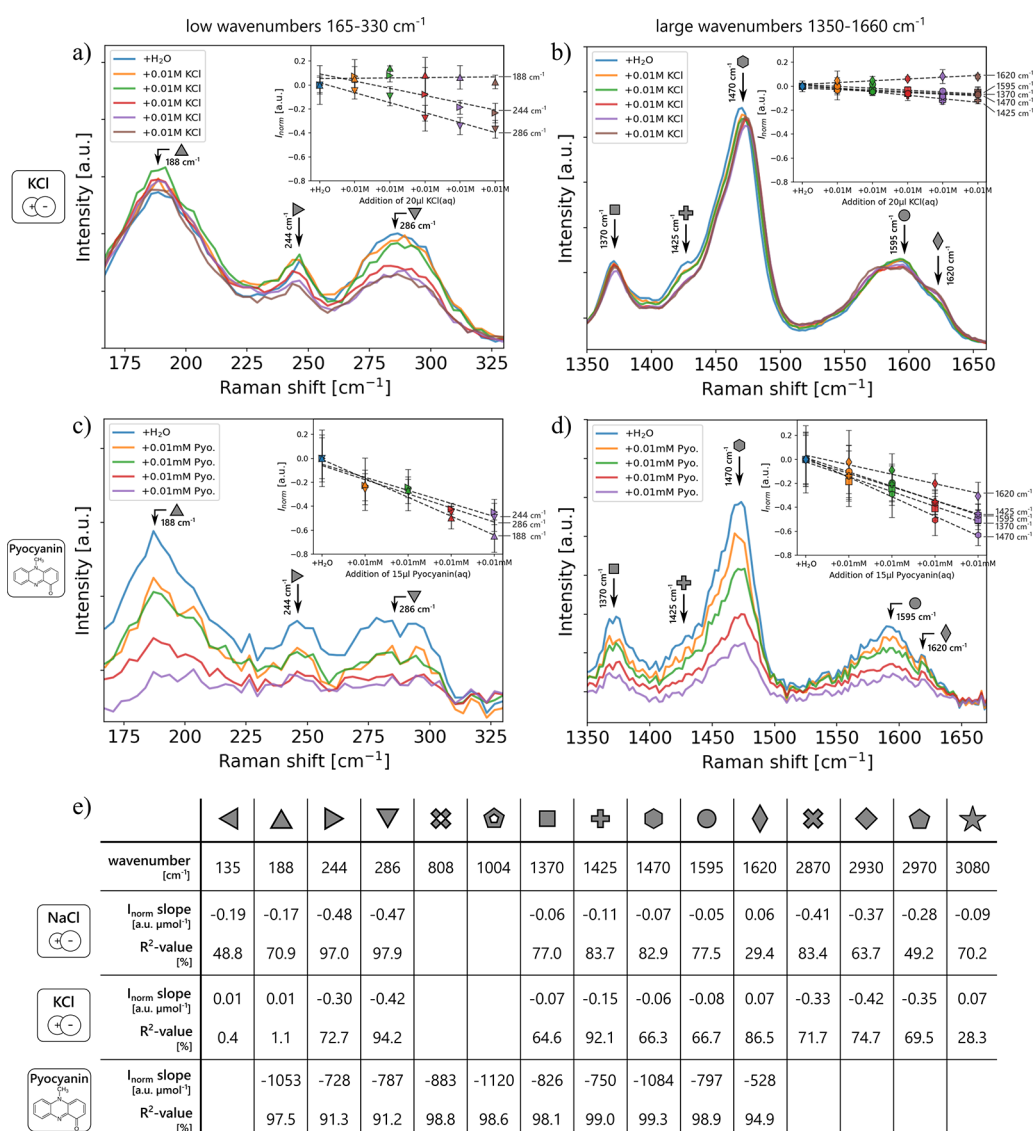
Figure 4. (a−d) Raman spectra of MOF@NC after successive treatment with H_2O and aqueous KCl (a, b) and pyocyanin solutions (c, d) (KCl, concentrations of 0.01 M, droplet volume of 20 μL; pyocyanin, concentrations of 0.01 mM, droplet volume of 15 μL). The low wavenumber region of 165−330 cm^{-1} and the large wavenumber region of 1350−1660 cm^{-1} are selected for comparison. Prominent peaks (marked with symbol and wavenumber) are fitted with a Lorentzian curve, and the normalized intensity change $I_{norm} = \Delta I/I_{H2O}$ (with $\Delta I = I − I_{H2O}$) of the peaks is evaluated and plotted against concentration, shown as inset. The error bars indicate the standard deviation, and the dashed lines show the linear fits. (e) Table comparing the normalized intensity changes $I_{norm} = \Delta I/I$ after treatment with the different aqueous analyte solutions NaCl, KCl, and pyocyanin. Slopes and R^2 values of the linear fits are given for all peaks.

of PEEK) was specially fabricated, in which the samples can be clamped and treated in a structured multiwell-like approach with different analytes and concentrations (Figure 2a). The porous and hydrophilic nature of the fibrous layers allows a good sample wetting with the aqueous solution, and at the same time, the NC layer provides a filtering effect as larger particles are physically retained. Small analytes with nanometer size can pass through the NC and may be trapped by interactions with the MOF, as indicated by changes in the Raman spectrum (Figure 2a).

First, six individual active samples were treated with solutions containing the ionic sweat biomarker sodium chloride (NaCl) of different concentrations, two of each with the same concentration (0.005 M, 0.05 M, and 0.5 M). Raman measurements were performed on MOF particles before and after addition of the solutions at different positions to confirm

statistical significance, in total 11−12 positions. The MOF particles can be spotted through the top NC fibrous layer, enabling a localization of the particle positions (Figure S9, Supporting Information). The full Raman spectra are shown in Figure 2b, which reveal a signal reduction for peaks (mainly in the marked regions of interest I, II, and III) at higher NaCl concentration. Zooming into region of interest I (low wavenumbers 120−340 cm^{-1}) in Figure 2c elucidates that the intensity shift does not occur equally for all peaks. The most pronounced intensity variation in this wavenumber window occurs at 286 cm (Figure 2d). The Raman intensities of the selected peak after different NaCl treatment conditions were fitted with a Lorentzian curve, and the intensity values were plotted against NaCl concentration, showing an exponential trend (Figure 2e). In the range of lower

concentrations (up to about 0.05 M), an approximately linear dependence was observed.

To quantify the intensity shift after NaCl addition, an active sample was treated successively with NaCl solution of equal concentration (0.01 M). Figure 3 shows the Raman spectra in the regions of interest I, II, and III, after sequential addition of deionized water and NaCl solution. The lines reflect the averaged spectra of three to six individual measurements (depending on the particle position) at different locations (individual spectra shown in Figure S10, full range spectra shown in Figure S11, Supporting Information). The most prominent peaks were fitted by a Lorentzian curve for each individual spectra (Figure S11, Supporting Information) and the normalized intensity change $I_{norm} = \Delta I / I_{H_2O}$ (with $\Delta I = I - I_{H_2O}$) was calculated and plotted against NaCl concentration, shown as insets in Figure 3. The sensitivity values, i.e., the slopes of the linear fits, were evaluated for each peak and presented together with coefficients of determination (R^2) in Figure 4e. The largest slope values of −0.48 and −0.47 au μmol^{-1} was observed to occur at the low wavenumber peaks at 244 and 286 cm^{-1}, respectively. Some peaks, e.g., at 1595 and 1370 cm^{-1}, showed a very weak change in normalized intensity of −0.05 and −0.06 au μmol^{-1}. There is also a weak change observed at 1620 cm^{-1} but with the difference that it has a positive sign (0.06 au μmol^{-1}) attributed to a peak shoulder whose intensity grows with increasing NaCl concentration. In Figure 3d, the relative intensity changes $I_{rel} = \Delta I / I$ for the peaks with the largest and smallest intensity reduction are shown for each wavenumber region of interest. It further illustrates the different sensitivities of the various peaks and highlights the stronger relative intensity change at the peaks 286 cm^{-1} (region I) and 2930 cm^{-1} (region III) compared to the peaks between 1350 and 1660 cm^{-1} (region II). Another observation is that the Raman spectrum did not alter after the addition of water following treatment with NaCl, so it can be assumed that no significant washing-out has occurred. The reproducibility of the results was tested and verified by treating another active sample with NaCl, increasing the salt concentration levels stepwise up to 0.5 M. The measured Raman spectra after each addition show a comparable intensity shift behavior for the similar low concentration range (Figure S12, Supporting Information). For high concentrations up to 0.5 M, a saturation effect is observed.

In addition to sodium chloride, potassium chloride (KCl) was also tested as a second ionic sweat biomarker on our sensing architecture. As previously, an active MOF@NC sample was successively treated with KCl solutions of equal concentration (0.01 M) and measured by Raman spectroscopy. The result shows similar behavior of intensity reduction as for treatment with NaCl, which becomes evident after evaluating the normalized and relative intensity changes and comparing the sensitivity values of the different peaks between NaCl and KCl (Figure 4 and Figure S13, Supporting Information). At this stage, a distinction between NaCl and KCl is not available from our data. It is possible that the negatively charged chloride ions present in both salts are responsible for the interaction with the MOF and thus the reason for the similar shift behavior of the two salts. Previous work shows the adsorption of iodine, also present as negatively charged I_2^- and I_3^-, into the pores of MOF-808 and their strong affinity toward the Zr cluster (strong adsorption by terminal −OH groups; only little affinity to BTC ligands).[61] It is not entirely clear whether the positively charged and chemically similar ions of

sodium and potassium have any effect on the vibrational modes of the MOF. What is currently clear is that the effect caused by the treatment of MOC@NC with the ionic solutions is visible by Raman spectroscopy. A deeper understanding of capture mechanism and interactions between analyte and MOF would require theoretical simulations, which is currently being worked on but which is beyond the scope of this paper. To further demonstrate the potential of our MOF sensor architecture for detecting not only ionic solutions but also small chemical molecules with biological relevance, pyocyanin, a biomarker for the pathogen *Pseudomonas aeruginosa* was selected to test the MOF sensor. Pyocyanin is water-soluble, and aqueous solutions were used for successive treatment of the active MOF@NC samples at equal concentrations (0.01 mM), which is in the concentration range found in biological fluids such as wound specimens, urine, or human ear secretions.[62] To reduce the fluorescence background and laser damage,[63] the laser excitation was changed to a longer wavelength of 785 nm (Figure S14, Supporting Information). The prominent MOF spectrum is readily measured with the longer wavelength and allows the analysis of signal reduction after addition of pyocyanin as shown in Figure 4b and Figure S15, Supporting Information. In comparison to the treatment with ionic solutions, the treatment with pyocyanin results not only in an intensity reduction of known peaks in the previous marked regions of interest but also in an intensity reduction of the peaks at wavenumbers 808 and 1004 cm^{-1}. It can be observed that the intensity decreases significantly more with increasing pyocyanin concentration for all peaks than for the ionic solutions. Figure 4 compares the zoomed-in Raman spectra for low wavenumbers (165−330 cm^{-1}) and for large wavenumbers (1350−1660 cm^{-1}) after treatment with KCl and pyocyanin. Here, the significantly stronger variation of the Raman spectrum after pyocyanin treatment, using a concentration lower by a factor of 1000 than for KCl, is clearly evident. The evaluation of the normalized intensity change and linear fitting expressed in numbers revealed the sensitivities for pyocyanin about 4 orders of magnitude larger than for the ionic NaCl and KCl solutions (Figure 4e). The largest slope value of −1120 au μmol^{-1} occurs at the strong intensity peak at 1004 cm^{-1}, followed closely by −1084 au μmol^{-1} at the peak at 1470 cm^{-1}, whose intensity hardly changes after KCl addition.

Since pyocyanin is not an ion but a small molecule that can interact with the MOF in a different way than ions, it can be expected that the influence on the MOF Raman spectrum differs from that of the treatment with salt solutions. The different effect is particularly noticeable for the wavenumbers 808 and 1004 cm^{-1}. The size of the pyocyanin molecule is small enough to enter the 18 Å wide pores of MOF-808[64] and interact with the Zr cluster or the organic linker. An exact mechanism of the interactions would again require theoretical simulations, but already pyocyanin can be distinguished from the ionic biomarkers. The fact that some arbitrary MOFs without specific functionality are already able to discriminate different types of biomarkers (small molecule vs ions) shows the great potential of Raman spectroscopy as a detection tool using our MOF@NC architecture as active element and could enable versatile chemical identification of specific analytes in the future by adjusting the MOF chemistry.

CONCLUSION

In summary, we have presented a method to effectively integrate MOF particles into a nitocellulose nanofibrous layer by electrospraying and electrospinning and realize a biocompatible MOF@NC membrane for the sensing of biomarkers in solution. Our approach has the advantage of keeping an open access to the MOF nanopores through the loose fiber mesh while ensuring a good physical particle entrapment as demonstrated by leaching tests. The samples were characterized using different methods such as SEM, AFM, EDX, and Raman spectroscopy before testing the sensing capability of the reported MOF architecture toward NaCl, KCl, and pyocyanin. In particular, we detected 4 orders of magnitude greater sensitivities for pyocyanin molecules than for the ionic biomarkers, suggesting that such a MOF-based architecture is not limited to only these components and can also be extended in the detection of more complex molecules such as α-synuclein,[65] tau,[66] and amyloid $\beta 40/42$[67] proteins present in solubilized buffer salt solutions and implicated in neurodegenerative disease pathologies. For future devices, the effects of strain warrant consideration when integrating MOFs with sensors for biochemical sensing.[68] Furthermore, the reported integration method is not only limited to MOF-808 but can be applied to MOFs in general with different functionality and tailored affinity for selected biomarkers, underlying the potential and flexibility of MOF@NC sensors.

EXPERIMENTAL METHODS

Materials. Nitrocellulose membrane was purchased from Merck (Sigma-Aldrich): Amersham Protran Western-blotting nitrocellulose membrane, article number GE106000112. MOF-808 was ordered and specially synthesized by novoMOF AG company (Untere Brühlstrasse 4, 4800 Zofingen, Switzerland). Pyocyanin (CAS no. 85-66-5, article number P0046-5MG) was purchased by Merck (Sigma-Aldrich).

Electrospraying of MOF-808 Particles. 0.2127 g of MOF-808 powder was suspended in 2 mL of isopropyl alcohol (IPA) in order to realize a 12 wt % particle suspension (wt % = $m_{MOF}/(m_{MOF} + m_{IPA})$). The suspension was treated by ultrasonication for at least 30 min, resulting in a milky liquid with well-dispersed MOF particles. The suspension was directly filled into a 2 mL syringe with a 18G blunt needle, which was then fixed in a syringe pump. A metal plate with attached substrate of choice (alumina foil or nitrocellulose membrane) was used as collector and placed with 15 cm distance to the needle opening. A high voltage of 20 kV was applied between the needle and the metal plate and the syringe pump flow rate was set to 120 μL/min, resulting in spraying of MOF particles on the substrate (environment temperature between 21 and 22 °C, relative humidity between 40% and 42%).

Electrospinning of Nitrocellulose. 0.365 g of nitrocellulose (NC) membrane was dissolved in a mixture of 2 mL of acetone and 1 mL of DMSO in order to realize a 12 wt % NC solution (wt % = $m_{NC}/(m_{NC} + m_{solvent})$). The solution was stirred for about 1 h, resulting in a clear and slightly yellowish NC solution. The solution was filled into a 2 mL syringe with a 18G blunt needle, which was then fixed in a syringe pump. A metal plate with attached substrate of choice (nitrocellulose membrane, potentially with dispersed MOF particles) was used as collector and placed with 15 cm distance to the needle opening. A high voltage of 21 kV was applied between the needle and the metal plate and the syringe pump flow rate was set to 10 μL/min, resulting in the release of a thin jet attracted to the electrode. During the time-of-flight, the solvent evaporated and thin NC fibers remained, which was deposited on the substrate (environment temperature between 21 and 22 °C, relative humidity between 40% and 42%).

X-ray Diffraction. MOF-808 powder was measured on a PANALYTICAL MPD instrument using a Bragg−Brentano setup using a Cu Kα radiation with λ = 1.5406 Å in the range of 2−80°. Data collection was performed at room temperature, and crystallite size could be derived using the Williamson−Hall approach. MOF-808 crystallographic data were obtained from Cambridge Crystallographic Data Center (CCDC): CSD entry is BOHWUS and deposition number is 1002672. Simulated XRD pattern and structure visualization were realized by CCDC Mercury software.

AFM Characterization. The AFM measurements were performed on active samples with integrated MOFs and on control samples with nitrocellulose fibers only, using a nanosurf NaniteAFM equipped with a tip scanner. The AFM probe was a Dyn190Al-10 cantilever (Nanosurf) with a tip apex radius of <10 nm, and the AFM scan was performed in tapping mode under standard laboratory conditions without temperature or environmental control (resonant frequency, 190 kHz; force constant, 48 N m^{-1}). The recorded AFM scan data (evaluated and leveled by Gwyddion software, version 2.58) showed the surface roughening of the active sample by the MOFs. In contrast, the control samples have a relatively uniform fibrous layer and line profile scans revealed an approximate thickness of up to 3 μm (Figure S6, Supporting Information).

Raman Spectroscopy. Raman spectra and corresponding optical images were acquired using a WITec Alpha 300R confocal Raman microscope with a 50× objective (Zeiss EC Epiplan-Neofluar Dic, NA = 0.55) and a 300 mm lens-based spectrometer (grating, 600 g mm^{-1}) equipped with a TE-cooled charge-coupled device (Andor Newton). Samples were measured in a closed chamber under a nitrogen atmosphere, where the samples were heated to 70 °C for 30 min at nitrogen flow prior to measurements to remove water and ensure consistent measurement conditions. The linearly polarized laser excitation had the wavelength λ_{exc} = 532 nm and a power of P = 20 mW read before the objective. Additional measurements with an excitation wavelength of λ_{exc} = 488 nm and grating with 1800 g mm^{-1} were performed to show the Raman signal at low wavenumbers of <1200 cm^{-1}. Pyocyanin measurements were performed with excitation wavelength of λ_{exc} = 785 nm and grating with 300 g mm^{-1}. 2D Raman maps of size 3 μm × 3 μm were acquired in backscattering geometry with an integration time of 5 s and a resolution of 2 pixels per μm. Single spectra were extracted by averaging the area scans and are displayed after cosmic ray removal and polynomial background subtraction. Normalization takes place at the 1004 cm^{-1} peak (for pyocyanin experiments at 1285 cm^{-1}) which shows no change after treatment, using the formula $(y - y_{min})/(y_{peak} - y_{min})$, with the intensity value y, the minimum intensity y_{min}, and the intensity value at the normalization peak y_{peak}.

ASSOCIATED CONTENT

ⓈI Supporting Information

The Supporting Information is available free of charge at https://pubs.acs.org/doi/10.1021/acsanm.2c05252.

> SEM images of MOF@NC, XRD, EDX, MOF-808 particles and nitrocellulose fibers image analysis, effect of ultrasonication time on MOF particles, AFM scans, leaching tests, Raman spectroscopy on different layers, optical microscopy images before and after NaCl (aq) treatment, additional Raman spectra after NaCl (aq) treatment (individual Raman spectra, full Raman spectra, Lorentzian fitting, larger concentration range), full Raman spectra after KCl (aq) treatment, full Raman spectra after pyocyanin (aq) treatment, optical microscopy images of laser damage on pyocyanin (PDF)

AUTHOR INFORMATION

Corresponding Authors

    Lars Lüder − *Empa, Swiss Federal Laboratories for Materials Science and Technology, Transport at Nanoscale Interfaces Laboratory, Dübendorf 8600, Switzerland; Department of*

Physics and Swiss Nanoscience Institute, University of Basel, Basel 4056, Switzerland; Empa, Swiss Federal Laboratories for Materials Science and Technology, Laboratory for Biomimetic Membranes and Textiles, St. Gallen 9014, Switzerland; ⬤ orcid.org/0000-0003-2799-7966; Email: lars.lueder@empa.ch

Michel Calame − Empa, Swiss Federal Laboratories for Materials Science and Technology, Transport at Nanoscale Interfaces Laboratory, Dübendorf 8600, Switzerland; Department of Physics and Swiss Nanoscience Institute, University of Basel, Basel 4056, Switzerland; ⬤ orcid.org/0000-0001-7467-9915; Email: michel.calame@empa.ch

Authors

Peter Niraj Nirmalraj − Empa, Swiss Federal Laboratories for Materials Science and Technology, Transport at Nanoscale Interfaces Laboratory, Dübendorf 8600, Switzerland; ⬤ orcid.org/0000-0002-2282-6781

Antonia Neels − Empa, Swiss Federal Laboratories for Materials Science and Technology, Center for X-ray Analytics, St. Gallen 9014, Switzerland; Department of Chemistry, University of Fribourg, Fribourg 1700, Switzerland; ⬤ orcid.org/0000-0001-5752-2852

René Michel Rossi − Empa, Swiss Federal Laboratories for Materials Science and Technology, Laboratory for Biomimetic Membranes and Textiles, St. Gallen 9014, Switzerland; Department of Health Science and Technology, ETH Zürich, Zürich 8092, Switzerland; ⬤ orcid.org/0000-0003-0946-682X

Complete contact information is available at:
https://pubs.acs.org/10.1021/acsanm.2c05252

Author Contributions

L.L., P.N.N., R.M.R., and M.C. conceived and designed the study. L.L. performed the sample fabrication, characterization, Raman measurements and sensing experiments. A.N. carried out the XRD experiments and analyzed the diffraction data. L.L., P.N.N., R.M.R., and M.C. performed and discussed the data analysis. L.L., P.N.N., R.M.R., and M.C. wrote the manuscript. All authors commented on the manuscript and provided critical feedback.

Notes

The authors declare no competing financial interest.

■ REFERENCES

(1) Yang, W.; Han, W.; Gao, H.; Zhang, L.; Wang, S.; Xing, L.; Zhang, Y.; Xue, X. Self-powered implantable electronic-skin for *in situ* analysis of urea/uric-acid in body fluids and the potential applications in real-time kidney-disease diagnosis. *Nanoscale* **2018**, *10* (4), 2099−2107.

(2) Yao, S.; Swetha, P.; Zhu, Y. Nanomaterial-enabled wearable sensors for healthcare. *Adv. Healthcare Mater.* **2018**, *7* (1), 1700889.

(3) Seshadri, D. R.; Li, R. T.; Voos, J. E.; Rowbottom, J. R.; Alfes, C. M.; Zorman, C. A.; Drummond, C. K. Wearable sensors for monitoring the internal and external workload of the athlete. *npj Digital Med.* **2019**, *2*, 71.

(4) Shi, Y.; Wei, X.; Wang, K.; He, D.; Yuan, Z.; Xu, J.; Wu, Z.; Wang, Z. L. Integrated All-Fiber Electronic Skin toward Self-Powered Sensing Sports Systems. *ACS Appl. Mater. Interfaces* **2021**, *13* (42), 50329−50337.

(5) Lim, H. B.; Ma, D.; Wang, B.; Kalbarczyk, Z.; Iyer, R. K.; Watkin, K. L. A Soldier Health Monitoring System for Military Applications. *Proceedings*, 2010 International Conference on Body Sensor Networks (BSN), June 2010; IEEE, 2010; pp 246−249.

(6) Shi, H.; Zhao, H.; Liu, Y.; Gao, W.; Dou, S.-C. Systematic Analysis of a Military Wearable Device Based on a Multi-Level Fusion Framework: Research Directions. *Sensors* **2019**, *19* (12), 2651.

(7) Nirmalraj, P. N.; Schneider, T.; Felbecker, A. Spatial organization of protein aggregates on red blood cells as physical biomarkers of Alzheimer's disease pathology. *Sci. Adv.* **2021**, *7* (39), No. eabj2137.

(8) Lee, H.; Hong, Y. J.; Baik, S.; Hyeon, T.; Kim, D. H. Enzyme-Based Glucose Sensor: From Invasive to Wearable Device. *Adv. Healthcare Mater.* **2018**, *7* (8), 1701150.

(9) Stern, E.; Vacic, A.; Rajan, N. K.; Criscione, J. M.; Park, J.; Ilic, B. R.; Mooney, D. J.; Reed, M. A.; Fahmy, T. M. Label-free biomarker detection from whole blood. *Nat. Nanotechnol.* **2010**, *5* (2), 138−142.

(10) Ryzhikova, E.; Ralbovsky, N. M.; Sikirzhytski, V.; Kazakov, O.; Halamkova, L.; Quinn, J.; Zimmerman, E. A.; Lednev, I. K. Raman spectroscopy and machine learning for biomedical applications: Alzheimer's disease diagnosis based on the analysis of cerebrospinal fluid. *Spectrochimica Acta Part A: Molecular and Biomolecular Spectroscopy* **2021**, *248*, 119188.

(11) Lekka, M.; Gil, D.; Pogoda, K.; Dulińska-Litewka, J.; Jach, R.; Gostek, J.; Klymenko, O.; Prauzner-Bechcicki, S.; Stachura, Z.; Wiltowska-Zuber, J.; Okoń, K.; Laidler, P. Cancer cell detection in tissue sections using AFM. *Arch. Biochem. Biophys.* **2012**, *518* (2), 151−156.

(12) Nyein, H. Y. Y.; Bariya, M.; Tran, B.; Ahn, C. H.; Brown, B. J.; Ji, W.; Davis, N.; Javey, A. A wearable patch for continuous analysis of thermoregulatory sweat at rest. *Nat. Commun.* **2021**, *12* (1), 1823.

(13) Wang, Z.; Hao, Z.; Wang, X.; Huang, C.; Lin, Q.; Zhao, X.; Pan, Y. A Flexible and Regenerative Aptameric Graphene-Nafion Biosensor for Cytokine Storm Biomarker Monitoring in Undiluted Biofluids toward Wearable Applications. *Adv. Funct. Mater.* **2021**, *31*, 2005958.

(14) Wang, Z.; Liu, T.; Yu, Y.; Asif, M.; Xu, N.; Xiao, F.; Liu, H. Coffee Ring-Inspired Approach toward Oriented Self-Assembly of Biomimetic Murray MOFs as Sweat Biosensor. *Small* **2018**, *14* (45), 1802670.

(15) Qiao, X.; Su, B.; Liu, C.; Song, Q.; Luo, D.; Mo, G.; Wang, T. Selective Surface Enhanced Raman Scattering for Quantitative Detection of Lung Cancer Biomarkers in Superparticle@MOF Structure. *Adv. Mater.* **2018**, *30* (5), 1702275.

(16) Vasilescu, A.; Hrinczenko, B.; Swain, G. M.; Peteu, S. F. Exhaled breath biomarker sensing. *Biosens. Bioelectron.* **2021**, *182*, 113193.

(17) Tan, W.; Sabet, L.; Li, Y.; Yu, T.; Klokkevold, P. R.; Wong, D. T.; Ho, C.-M. Optical protein sensor for detecting cancer markers in saliva. *Biosens. Bioelectron.* **2008**, *24* (2), 266−271.

(18) Mani, V.; Beduk, T.; Khushaim, W.; Ceylan, A. E.; Timur, S.; Wolfbeis, O. S.; Salama, K. N. Electrochemical sensors targeting salivary biomarkers: A comprehensive review. *TrAC Trends in Analytical Chemistry* **2021**, *135*, 116164.

(19) Pusta, A.; Tertiş, M.; Cristea, C.; Mirel, S. Wearable Sensors for the Detection of Biomarkers for Wound Infection. *Biosensors* **2022**, *12* (1), 1.

(20) Gianino, E.; Miller, C.; Gilmore, J. Smart Wound Dressings for Diabetic Chronic Wounds. *Bioengineering* **2018**, *5* (3), 51.

(21) Terse-Thakoor, T.; Punjiya, M.; Matharu, Z.; Lyu, B.; Ahmad, M.; Giles, G. E.; Owyeung, R.; Alaimo, F.; Shojaei Baghini, M.; Brunyé, T. T.; Sonkusale, S. Thread-based multiplexed sensor patch for real-time sweat monitoring. *npj Flexible Electron.* **2020**, *4* (1), 18.

(22) Escobedo, P.; Fernández-Ramos, M. D.; López-Ruiz, N.; Moyano-Rodríguez, O.; Martínez-Olmos, A.; Pérez de Vargas-Sansalvador, I. M.; Carvajal, M. A.; Capitán-Vallvey, L. F.; Palma,

A. J. Smart facemask for wireless CO2 monitoring. *Nat. Commun.* **2022**, *13* (1), 72.

(23) Liu, X.; Lillehoj, P. B. Embroidered electrochemical sensors on gauze for rapid quantification of wound biomarkers. *Biosens. Bioelectron.* **2017**, *98*, 189−194.

(24) Jankowska, D. A.; Bannwarth, M. B.; Schulenburg, C.; Faccio, G.; Maniura-Weber, K.; Rossi, R. M.; Scherer, L.; Richter, M.; Boesel, L. F. Simultaneous detection of pH value and glucose concentrations for wound monitoring applications. *Biosens. Bioelectron.* **2017**, *87*, 312−319.

(25) Jayathilaka, W. A. D. M.; Qi, K.; Qin, Y.; Chinnappan, A.; Serrano-García, W.; Baskar, C.; Wang, H.; He, J.; Cui, S.; Thomas, S. W.; Ramakrishna, S. Significance of Nanomaterials in Wearables: A Review on Wearable Actuators and Sensors. *Adv. Mater.* **2019**, *31* (7), 1805921.

(26) Hoskins, B. F.; Robson, R. Design and construction of a new class of scaffolding-like materials comprising infinite polymeric frameworks of 3D-linked molecular rods. A reappraisal of the zinc cyanide and cadmium cyanide structures and the synthesis and structure of the diamond-related frameworks [N(CH3)4][CuIZnII(CN)4] and CuI[4,4′,4″,4‴-tetracyanotetraphenylmethane]-BF4.xC6H5NO2. *J. Am. Chem. Soc.* **1990**, *112* (4), 1546−1554.

(27) Yaghi, O. M.; Li, H. Hydrothermal Synthesis of a Metal-Organic Framework Containing Large Rectangular Channels. *J. Am. Chem. Soc.* **1995**, *117* (41), 10401−10402.

(28) Hönicke, I. M.; Senkovska, I.; Bon, V.; Baburin, I. A.; Bönisch, N.; Raschke, S.; Evans, J. D.; Kaskel, S. Balancing Mechanical Stability and Ultrahigh Porosity in Crystalline Framework Materials. *Angew. Chem., Int. Ed.* **2018**, *57* (42), 13780−13783.

(29) Chen, Z.; Li, P.; Anderson, R.; Wang, X.; Zhang, X.; Robison, L.; Redfern, L. R.; Moribe, S.; Islamoglu, T.; Gómez-Gualdrón, D. A.; Yildirim, T.; Stoddart, J. F.; Farha, O. K. Balancing volumetric and gravimetric uptake in highly porous materials for clean energy. *Science* **2020**, *368* (6488), 297−303.

(30) Eddaoudi, M.; Kim, J.; Rosi, N.; Vodak, D.; Wachter, J.; O'Keeffe, M.; Yaghi, O. M. Systematic Design of Pore Size and Functionality in Isoreticular MOFs and Their Application in Methane Storage. *Science* **2002**, *295* (5554), 469−472.

(31) Zhang, Y.; Yuan, S.; Feng, X.; Li, H.; Zhou, J.; Wang, B. Preparation of Nanofibrous Metal-Organic Framework Filters for Efficient Air Pollution Control. *J. Am. Chem. Soc.* **2016**, *138* (18), 5785−5788.

(32) Peng, Y.; Huang, H.; Zhang, Y.; Kang, C.; Chen, S.; Song, L.; Liu, D.; Zhong, C. A versatile MOF-based trap for heavy metal ion capture and dispersion. *Nat. Commun.* **2018**, *9* (1), 187.

(33) Cheng, W.; Tang, X.; Zhang, Y.; Wu, D.; Yang, W. Applications of metal-organic framework (MOF)-based sensors for food safety: Enhancing mechanisms and recent advances. *Trends in Food Science & Technology* **2021**, *112*, 268−282.

(34) Xu, Q.-Y.; Tan, Z.; Liao, X.-W.; Wang, C. Recent advances in nanoscale metal-organic frameworks biosensors for detection of biomarkers. *Chin. Chem. Lett.* **2022**, *33* (1), 22−32.

(35) Kreno, L. E.; Leong, K.; Farha, O. K.; Allendorf, M.; Van Duyne, R. P.; Hupp, J. T. Metal-Organic Framework Materials as Chemical Sensors. *Chem. Rev.* **2012**, *112* (2), 1105−1125.

(36) Wang, H.-S.; Wang, Y.-H.; Ding, Y. Development of biological metal-organic frameworks designed for biomedical applications: from bio-sensing/bio-imaging to disease treatment. *Nanoscale Adv.* **2020**, *2* (9), 3788−3797.

(37) Yang, J.; Yang, Y. W. Metal-Organic Frameworks for Biomedical Applications. *Small* **2020**, *16* (10), 1906846.

(38) Yeung, H. H. M.; Yoshikawa, G.; Minami, K.; Shiba, K. Strain-based chemical sensing using metal-organic framework nanoparticles. *Journal of Materials Chemistry A* **2020**, *8* (35), 18007−18014.

(39) Guo, Z.; Florea, A.; Cristea, C.; Bessueille, F.; Vocanson, F.; Goutaland, F.; Zhang, A.; Săndulescu, R.; Lagarde, F.; Jaffrezic-Renault, N. 1,3,5-Trinitrotoluene detection by a molecularly imprinted polymer sensor based on electropolymerization of a microporous-metal-organic framework. *Sens. Actuators, B* **2015**, *207*, 960−966.

(40) Hu, M.; Zhu, L.; Li, Z.; Guo, C.; Wang, M.; Wang, C.; Du, M. CoNi bimetallic metal-organic framework as an efficient biosensing platform for miRNA 126 detection. *Appl. Surf. Sci.* **2021**, *542*, 148586.

(41) Anik, D. C.; Timur, S.; Dursun, Z. Metal organic frameworks in electrochemical and optical sensing platforms: a review. *Microchim. Acta* **2019**, *186* (3), 196.

(42) Zhang, Z.; Ji, H.; Song, Y.; Zhang, S.; Wang, M.; Jia, C.; Tian, J.-Y.; He, L.; Zhang, X.; Liu, C.-S. Fe(III)-based metal-organic framework-derived core-shell nanostructure: Sensitive electrochemical platform for high trace determination of heavy metal ions. *Biosens. Bioelectron.* **2017**, *94*, 358−364.

(43) Trino, L. D.; Albano, L. G. S.; Granato, D. C.; Santana, A. G.; de Camargo, D. H. S.; Correa, C. C.; Bof Bufon, C. C.; Paes Leme, A. F. ZIF-8 Metal-Organic Framework Electrochemical Biosensor for the Detection of Protein-Protein Interaction. *Chem. Mater.* **2021**, *33* (4), 1293−1306.

(44) Guo, C.; Hu, M.; Li, Z.; Duan, F.; He, L.; Zhang, Z.; Marchetti, F.; Du, M. Structural hybridization of bimetallic zeolitic imidazolate framework (ZIF) nanosheets and carbon nanofibers for efficiently sensing α-synuclein oligomers. *Sens. Actuators, B* **2020**, *309*, 127821.

(45) Raman, C. V. A change of wave-length in light scattering. *Nature* **1928**, *121* (3051), 619−619.

(46) Chung, M.; Skinner, W. H.; Robert, C.; Campbell, C. J.; Rossi, R. M.; Koutsos, V.; Radacsi, N. Fabrication of a Wearable Flexible Sweat pH Sensor Based on SERS-Active Au/TPU Electrospun Nanofibers. *ACS Appl. Mater. Interfaces* **2021**, *13* (43), 51504−51518.

(47) Dybas, J.; Alcicek, F. C.; Wajda, A.; Kaczmarska, M.; Zimna, A.; Bulat, K.; Blat, A.; Stepanenko, T.; Mohaissen, T.; Szczesny-Malysiak, E.; Perez-Guaita, D.; Wood, B. R.; Marzec, K. M. Trends in biomedical analysis of red blood cells - Raman spectroscopy against other spectroscopic, microscopic and classical techniques. *TrAC Trends in Analytical Chemistry* **2022**, *146*, 116481.

(48) Matthiae, M.; Zhu, X.; Marie, R.; Kristensen, A. In-line whole blood fractionation for Raman analysis of blood plasma. *Analyst* **2019**, *144* (2), 602−610.

(49) Dharmalingam, P.; Venkatakrishnan, K.; Tan, B. Probing Cancer Metastasis at a Single-Cell Level with a Raman-Functionalized Anionic Probe. *Nano Lett.* **2020**, *20* (2), 1054−1066.

(50) Devitt, G.; Howard, K.; Mudher, A.; Mahajan, S. Raman Spectroscopy: An Emerging Tool in Neurodegenerative Disease Research and Diagnosis. *ACS Chem. Neurosci.* **2018**, *9* (3), 404−420.

(51) Davis, B. M.; Hemphill, A. J.; Cebeci Maltaş, D.; Zipper, M. A.; Wang, P.; Ben-Amotz, D. Multivariate Hyperspectral Raman Imaging Using Compressive Detection. *Anal. Chem.* **2011**, *83* (13), 5086−5092.

(52) Guevara, E.; Torres-Galván, J. C.; Ramírez-Elías, M. G.; Luevano-Contreras, C.; González, F. J. Use of Raman spectroscopy to screen diabetes mellitus with machine learning tools. *Biomed. Opt. Express* **2018**, *9* (10), 4998.

(53) Jermyn, M.; Mok, K.; Mercier, J.; Desroches, J.; Pichette, J.; Saint-Arnaud, K.; Bernstein, L.; Guiot, M.-C.; Petrecca, K.; Leblond, F. Intraoperative brain cancer detection with Raman spectroscopy in humans. *Sci. Transl. Med.* **2015**, *7* (274), 274ra19.

(54) Sun, H.; Cong, S.; Zheng, Z.; Wang, Z.; Chen, Z.; Zhao, Z. Metal-Organic Frameworks as Surface Enhanced Raman Scattering Substrates with High Tailorability. *J. Am. Chem. Soc.* **2019**, *141* (2), 870−878.

(55) Sonner, Z.; Wilder, E.; Heikenfeld, J.; Kasting, G.; Beyette, F.; Swaile, D.; Sherman, F.; Joyce, J.; Hagen, J.; Kelley-Loughnane, N.; Naik, R. The microfluidics of the eccrine sweat gland, including biomarker partitioning, transport, and biosensing implications. *Biomicrofluidics* **2015**, *9* (3), 031301.

(56) Li, Y.; Hu, Y.; Chen, T.; Chen, Y.; Li, Y.; Zhou, H.; Yang, D. Advanced detection and sensing strategies of Pseudomonas aeruginosa and quorum sensing biomarkers: A review. *Talanta* **2022**, *240*, 123210.

(57) Samy, M.; Ibrahim, M. G.; Fujii, M.; Diab, K. E.; ElKady, M.; Gar Alalm, M. CNTs/MOF-808 painted plates for extended treatment of pharmaceutical and agrochemical wastewaters in a novel photocatalytic reactor. *Chem. Eng. J.* **2021**, *406*, 127152.

(58) Biswas, S.; Lan, Q.; Xie, Y.; Sun, X.; Wang, Y. Label-Free Electrochemical Immunosensor for Ultrasensitive Detection of Carbohydrate Antigen 125 Based on Antibody-Immobilized Biocompatible MOF-808/CNT. *ACS Appl. Mater. Interfaces* **2021**, *13* (2), 3295−3302.

(59) Himabindu, B.; Latha Devi, N. S. M. P.; Rajini Kanth, B. Microstructural parameters from X-ray peak profile analysis by Williamson-Hall models; A review. *Materials Today: Proceedings* **2021**, *47*, 4891−4896.

(60) López-López, M.; Delgado, J. J.; García-Ruiz, C. Ammunition Identification by Means of the Organic Analysis of Gunshot Residues Using Raman Spectroscopy. *Anal. Chem.* **2012**, *84* (8), 3581−3585.

(61) Chen, P.; He, X.; Pang, M.; Dong, X.; Zhao, S.; Zhang, W. Iodine Capture Using Zr-Based Metal-Organic Frameworks (Zr-MOFs): Adsorption Performance and Mechanism. *ACS Appl. Mater. Interfaces* **2020**, *12* (18), 20429−20439.

(62) Wu, X.; Chen, J.; Li, X.; Zhao, Y.; Zughaier, S. M. Culture-free diagnostics of Pseudomonas aeruginosa infection by silver nanorod array based SERS from clinical sputum samples. *Nanomedicine: Nanotechnology, Biology and Medicine* **2014**, *10* (8), 1863−1870.

(63) Yang, S.; Li, B.; Slipchenko, M. N.; Akkus, A.; Singer, N. G.; Yeni, Y. N.; Akkus, O. Laser wavelength dependence of background fluorescence in Raman spectroscopic analysis of synovial fluid from symptomatic joints: Analysis of synovial fluid from symptomatic joints. *J. Raman Spectrosc.* **2013**, *44* (8), 1089−1095.

(64) Plessers, E.; Fu, G.; Tan, C.; De Vos, D.; Roeffaers, M. Zr-Based MOF-808 as Meerwein-Ponndorf-Verley Reduction Catalyst for Challenging Carbonyl Compounds. *Catalysts* **2016**, *6* (7), 104.

(65) Synhaivska, O.; Bhattacharya, S.; Campioni, S.; Thompson, D.; Nirmalraj, P. N. Single-Particle Resolution of Copper-Associated Annular α-Synuclein Oligomers Reveals Potential Therapeutic Targets of Neurodegeneration. *ACS Chem. Neurosci.* **2022**, *13* (9), 1410−1421.

(66) Wegmann, S.; Medalsy, I. D.; Mandelkow, E.; Müller, D. J. The fuzzy coat of pathological human Tau fibrils is a two-layered polyelectrolyte brush. *Proc. Natl. Acad. Sci. U. S. A.* **2013**, *110* (4), No. E313-E321.

(67) Nirmalraj, P. N.; List, J.; Battacharya, S.; Howe, G.; Xu, L.; Thompson, D.; Mayer, M. Complete aggregation pathway of amyloid β (1−40) and (1−42) resolved on an atomically clean interface. *Science Advances* **2020**, *6* (15), No. eaaz6014.

(68) Yuan, H.; Li, N.; Fan, W.; Cai, H.; Zhao, D. Metal-Organic Framework Based Gas Sensors. *Advanced Science* **2022**, *9* (6), 2104374.

📖 Recommended by ACS

Mixed Matrix Membranes Based on ZIF-8 Nanoparticles/Poly(4-styrene sulfonate) Fillers for Enhanced CO₂ Separation

Chao Liang, Zhong Wei, *et al.*

FEBRUARY 15, 2023
ACS APPLIED NANO MATERIALS　　　READ ☑

Flame-Retardant and Form-Stable Delignified Wood-Based Phase Change Composites with Superior Energy Storage Density and Reversible Thermochromic Properties for Visu...

Jiuao Wang, Xiaosheng Du, *et al.*

FEBRUARY 17, 2023
ACS SUSTAINABLE CHEMISTRY & ENGINEERING　　　READ ☑

Al/CuF₂ Composite Materials with Ignition Characteristics and Pressure Output Ability for Nanothermites

Jie Ji, Xiaode Guo, *et al.*

FEBRUARY 08, 2023
ACS APPLIED NANO MATERIALS　　　READ ☑

Film-Formation and Binder-Free Pigment Printing of Fluorosilicone-Modified Polyacrylate/Pigment Hybrid Latex: Effect of Cross-Linking Degree

Lin Lu, Dongming Qi, *et al.*

FEBRUARY 13, 2023
ACS APPLIED POLYMER MATERIALS　　　READ ☑

Get More Suggestions >